International Journal of Coal Science & Technology (2025) 12:6
https://doi.org/10.1007/s40789-025-00752-x

RESEARCH

Analysis on the dust prevention mechanism of air curtain in fully mechanized excavation tunnel

Hao Wang[1,2] · Chuangye Xin[1] · Shouqing Lu[1,2] · Yongliang Zhang[1,2] · Zhanyou Sa[1,2] · Jinxu Tao[1] · Zhuang Liu[1]

Received: 1 October 2023 / Revised: 14 January 2024 / Accepted: 6 January 2025
© The Author(s) 2025

Abstract
Aiming at reducing the dust pollution during the tunneling process and improving the application efficiency of air curtain dust prevention technology, according to the changes of radial jet velocity (v_r), axial extraction velocity (v_e) and extraction distance (L) in the formation process of air curtain, the numerical simulation method was used to analyze the rules of airflow structure evolution and the diffusion characteristics of dust particles in fully mechanized excavation tunnel. The results indicate that as v_r and v_e increase, the migration path of the wall jet of the air curtain changes into an axial direction; as L decreases, the migration distance increases accordingly. These phenomena make the airflow distribution in the working face tends to be uniform. The dust diffusion distance reduces as well, wherein, the range of the discrete area of dust particles decreases sharply, until all dust particles are concentrated in the accumulation area. On this basis, the v_r, v_e and L were optimized and applied in the $63_{up}08$ fully mechanized working face. By the application of the optimal parameters, the average dust removal efficiency at the driver's position increased by 71%. The dust concentration was reduced and the working environment had been improved effectively.

Keywords Air curtain · Dust prevention mechanism · Airflow structure evolution · Dust diffusion · Fully mechanized excavation tunnel

1 Introduction

In China, the rapid growth of the consumption of mineral resources causes a significantly increase of the output of coal. Large-scale fully mechanized mining equipment is widely used in coal mines. This has led to a rapid increase in the mining speed, and as a result, the high concentration dust pollution has become increasingly severe (Jiang and Luo 2021). In the underground space, the fully mechanized excavation tunnel provides basic conditions for coal mining and transportation. It is an extremely important production site. The dust generated by coal cutting in the working face accounts for more than 85% of the dust generated by all procedures in the fully mechanized excavation tunnel. In the underground space, the high concentration dust pollution is an important factor that leads to miners' pneumoconiosis (Shekarian et al. 2021; Trechera et al. 2022; Fan and Liu 2021; Ren et al. 2020; Agioutanti et al. 2020). As shown in Fig. 1, from 2011 to 2020, the accumulative number of occupational pneumoconiosis cases has reached 227,139 in China, accounting for 87% of the total cases of occupational disease. The number of mining-related pneumoconiosis cases accounting for about 90% of the total number of occupational pneumoconiosis cases (Nie et al. 2022; Gu et al., 2021).

As the fully mechanized excavation tunnel is a semi-closed space with a single passage, inefficient local ventilation can easily make dust mix with fresh airflow, causing serious dust pollution (Geng et al. 2019; Gao et al. 2021; Animah et al. 2024). Under this circumstance, clarifying the dust prevention mechanism of local ventilation system and selecting optimal ventilation parameters are essential to fundamentally solve the dust pollution problem (Aznar-Sánchez et al. 2019; Lodhia and Hess 2014). Researchers believe that air curtains can be developed to block dust.

✉ Hao Wang
wanghaojx@qut.edu.cn

[1] Department of Safety Science and Engineering, Qingdao University of Technology, Qingdao 266520, China

[2] Research Center for Accident Prevention Technology in Key Industries of Shandong Province, Qingdao University of Technology, Qingdao 266520, China

Published online: 28 January 2025

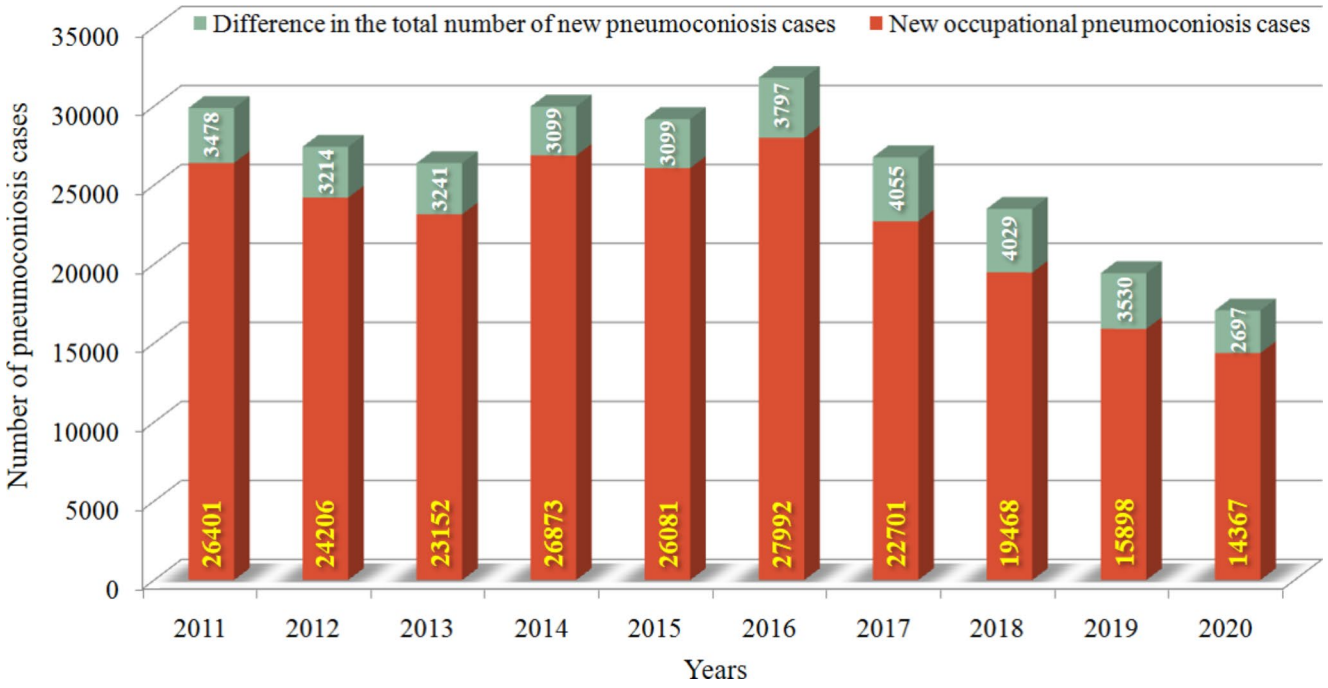

Fig. 1 Cases of new occupational disease in China

Because the transparent air curtain do not cause visual obstruction and can also isolate personnel working regions from dust producing region (Wang et al. 2021a; Geng et al. 2018; Jiang et al. 2015). German researchers developed an air curtain device to generate a single linear air curtain (Nie et al. 2016; Guyonnaud et al. 2000). Wang et al. (2019a); Li et al. (2019b) carried out model experiment and numerical simulation on the distributions of airflow and dust concentration in tunnels with single radial air curtains. They achieved the optimal air volume, structure and installation position of air curtain device. This study provides a theoretical basis for the optimization design of the air curtain device and its application. Zhang et al. (2011) established a new type of air curtain dust removal system by the utilization of air curtain fan. Using numerical simulation to analyze the airflow streamlines and dust particle traces under different airflow velocities, dust removal pipe diameters and outlet pressures. The impact rule of the above variables on the dust removal system was obtained. The conclusions has guiding significance for the structural optimization of the air curtain dust removal system. Kurnia et al. (2015) developed a hybrid vibration system that combined physical vibration with air curtain to reduce dust dispersion in the working face. A dynamic model was established using the Euler-Lagrange method to track the diffusion of dust particles, and the optimal mixed vibration scheme was obtained. Ge et al. (2003) invented an air curtain fan to form a jet convergence field, enveloping the pollution source. This study analyzed the structure and operating mechanism of the fan, established a mathematical model to describe its flow field, and carried out typical applications. The achievement provides practical reference for in-depth research and renovation of air curtain devices. Cheng et al. (2016) designed a new air curtain device that could form multi-directional radial jets. The air curtain could cover the entire section of the tunnel and has been widely promoted and applied in fully mechanized excavation tunnels in coal mines. Yin et al. (2019); Hua et al. (2020); Wang et al. (2021b) based on the new air curtain device, further analyzed the airflow migration and dust diffusion under different pressure air volumes and air curtain positions through numerical simulation and obtained optimal parameters. These studies provide theoretical guidance for the efficient application of the multi-directional air curtain.

The above-mentioned achievements have conducted extensive and in-depth research on the development and optimization of air curtain devices, changes in air curtain forms, and the effects of various airflow parameters and air curtain positions on dust concentration distribution. They have played a very important role in promoting the development and application of air curtain dust prevention technology. However, at present, the air curtain dust prevention has not achieved ideal effect. The main reason is that the air curtain migration is a dynamic process, the difference in axial and radial velocities and migration distances of the air curtain will directly affect the airflow structure along the way, resulting in completely different distribution patterns of dust particles. But the existing research achievements

rarely consider the impact of air curtain migration on the evolution of airflow structure in the tunnel, which leads to the unclear dust prevention mechanism of air curtain and insufficient theoretical basis for on-site application.

Numerical simulation, experiment, field measurement are the commonly used theoretical research methods (Parra et al. 2006). Among them, numerical simulation comprehensively restores the production environment through proportional physical models, and uses various visual images to display the details of the flow field, greatly improving the efficiency of flow field analysis (Hu et al. 2019; Ding et al. 2017). Experiment is difficult to restore the actual production environment due to the constraints of equipment and site scale, and the test process is very complicated (Li et al. 2016, 2019a). Field measurement is restricted by the operation process, but the measured results are the most able to reflect the actual situation and have the most reference value (Wang et al. 2018; Lu et al. 2022).

Based on the above, a typical fully mechanized excavation tunnel, the $63_{up}08$ excavation tunnel in Dongtan Coal Mine of Shandong Energy Group Co., Ltd. was taken as the study object, the combined method of numerical simulation and field measurement was utilized to conduct the analysis on the dust prevention mechanism of air curtain under various radial jet velocities, axial extraction velocities and extraction distances in fully mechanized excavation tunnel. The conclusions can provide theoretical guidance for the exact dust pollutant treatment in the underground excavation tunnel.

2 Model establishment

2.1 Mathematical model

In the fully mechanized excavation tunnel, the dust volume fraction contained in the airflow is less than 20%, the interaction between dust particles and the impact of dust particles on the airflow can be ignored (Shi et al. 2017; Zhou et al. 2020; Kumar et al. 2022). In this study, the Reynolds time-averaged formula based on the Euler coordinate system is used to describe the turbulent migration of airflow. The stochastic orbital tracking method based on the Lagrangian coordinate system is used to describe the dust diffusion process (Magesh et al. 2016).

It is assumed that the airflow is an incompressible fluid, the governing formulas include the continuity formula and the momentum formula (Zhang et al. 2021; Ding 2020).

Continuity formula:

$$\frac{\partial}{\partial x_i}(\rho u_i) = 0 \tag{1}$$

Momentum formula:

$$\begin{aligned}\frac{\partial}{\partial x_j}(\rho u_i u_j) &= -\frac{\partial p}{\partial x_i} + \rho g_i \\ &+ \frac{\partial}{\partial x_j}\left[(\mu + \mu_t)\left(\frac{\partial u_i}{\partial x_j} + \frac{\partial u_j}{\partial x_i}\right)\right]\end{aligned} \tag{2}$$

The air curtain belongs to a wall jet and the swirling flow is strong. The Realizable κ-ε model is more suitable for the simulation of a mixed flow on a plane. Therefore, the Realizable κ-ε model was selected in this study (Ding 2020).

κ formula:

$$\frac{\partial(\rho\kappa)}{\partial t} + \frac{\partial(\rho\kappa u_i)}{\partial x_i} = \frac{\partial}{\partial x_j}\left[\left(\mu + \frac{\mu_t}{\sigma_\kappa}\right)\frac{\partial \kappa}{\partial x_j}\right] + G_\kappa - \rho\varepsilon \tag{3}$$

ε formula:

$$\begin{aligned}&\frac{\partial(\rho\varepsilon)}{\partial t} + \frac{\partial(\rho\varepsilon u_i)}{\partial x_i} \\ &= \frac{\partial}{\partial x_j}\left[\left(\mu + \frac{\mu_t}{\sigma_\varepsilon}\right)\frac{\partial \varepsilon}{\partial x_j}\right] \\ &+ \rho C_1 E\varepsilon \\ &- \rho C_2 \frac{\varepsilon^2}{\kappa + \sqrt{v\varepsilon}}\end{aligned} \tag{4}$$

where ρ is air density, kg/m^3; u is time-averaged velocity of x direction, m/s; x_i, x_j are coordinate positions, the subscripts i, j represent x, y, z directions with values of 1, 2, 3; p is valid turbulence pressure, Pa; μ is fluid viscosity coefficient, Pa·s; μ_t is turbulent viscosity coefficient, Pa·s; κ is turbulence kinetic energy, J; t is time, s; σ_κ is the Turbulence Prandtl number for κ formula, takes constant terms with 1.0; G_κ is the generated turbulence kinetic energy caused by velocity gradients; ε is dissipation rate of turbulence kinetic energy; σ_ε is the Turbulence Prandtl number for ε formula, takes constant terms with 1.2; C_1 takes constant terms with 1.4; C_2 takes constant terms with 1.9; v is average velocity, m/s.

The DPM model was used to integrat the force balance formula and calculate the dust migration trajectory in a Lagrange coordinate system (Wang et al. 2019b). The force balance formula is as follows:

$$\frac{\mathrm{d}u_\mathrm{p}}{\mathrm{d}t} = F_\mathrm{d} + \frac{g(\rho_\mathrm{p} - \rho)}{\rho_\mathrm{p}} + F \tag{5}$$

Where u_p is particle velocity, m/s; F_d is drag force per unit particle mass, N; ρ_p is density of dust particle, kg/m^3; F is

other forces acting on the dust particles, N; F has a very small order of magnitude and can be ignored in the numerical simulation.

In addition to the acting force, the dust migration trajectories are also subject to turbulence in the airflow. To describe the turbulent diffusion of dust, by using the random trajectory tracking method and utilizing the instantaneous velocity of the airflow, the equilibrium formula for the interaction of a single dust particle is integrated. When the number of integrated dust particles is sufficient, the calculation results can reflect the random effect of turbulence on dust diffusion.

2.2 Physical model

To truly reflect the working environment, a proportional physical model of the $63_{up}08$ fully mechanized excavation tunnel was established by Solidworks 2021. As shown in Fig. 2, the tunnel is a cuboid of Length×Wideth×Height =80 m×5.54 m×3.8 m. There is a roadheader, a pressing air duct, an extraction air duct, a wall-attached air duct, a dedusting fan, a stage loader, and a belt loader in the tunnel. The air ducts have a same diameter of 0.8 m; the central axes of the air ducts are all 2.8 m above the floor. The pressing air outlet and the radial jet ports are 10 m and 20 m from the working face, respectively. The wall-attached air duct contains ten groups of radial jet ports (T_1~T_{10}). The ports of A and C styles are arranged toward the roof, B and E styles are arranged toward the floor, D style is arranged horizontally toward the inside space. To avoid the interference of model changes on the simulation results, for models with different extraction distances, only the position of the inlet of the extraction air duct was changed. There were no changes made in sizes or positions of any equipment.

Since it is difficult to replicate the details, the simulation was simplified and assumed as follows: (1) the air was idealized as an incompressible continuous fluid, the small internal facilities were not reflected in the calculation domain; (2) the velocity at the inlet and outlet was uniform, the airflow was in a fully turbulent state; (3) the change of the temperature was not considered; (4) the interaction between particles was ignored.

3 Mesh and boundary condition

3.1 Mesh generation

The physical models were meshed by ICEM. According to the complexity of the model, the unstructured tetrahedral mesh was chosen for the fluid domain division. The mesh size could directly affect the mesh quality and the accuracy of numerical simulation. According to Yin et al. (2020) and Zhang et al. (2020), a comparative analysis was conducted on the airflow velocity at the same measurement point under different mesh sizes to verify the independence of the mesh. The mesh size suitable for numerical simulation was selected as well. This study adopted the same method to conduct mesh independence test. Taking the model with the extraction distance of 2 m as an example, with 0.3 m, 0.2 m and 0.1 m as the maximum mesh size, three different meshes were obtained: large meshes (total number: 1,637,036), medium meshes (total number: 3,184,042), small meshes (total number: 24,711,267).

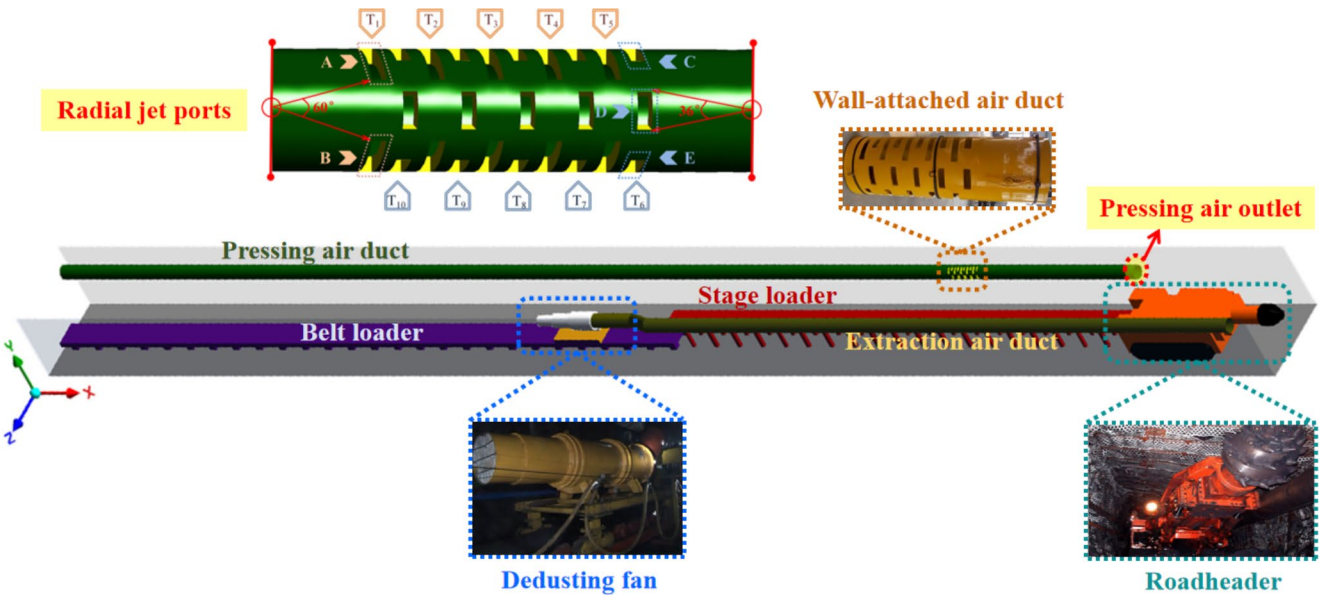

Fig. 2 Proportional physical model of the $63_{up}08$ fully mechanized excavation tunnel

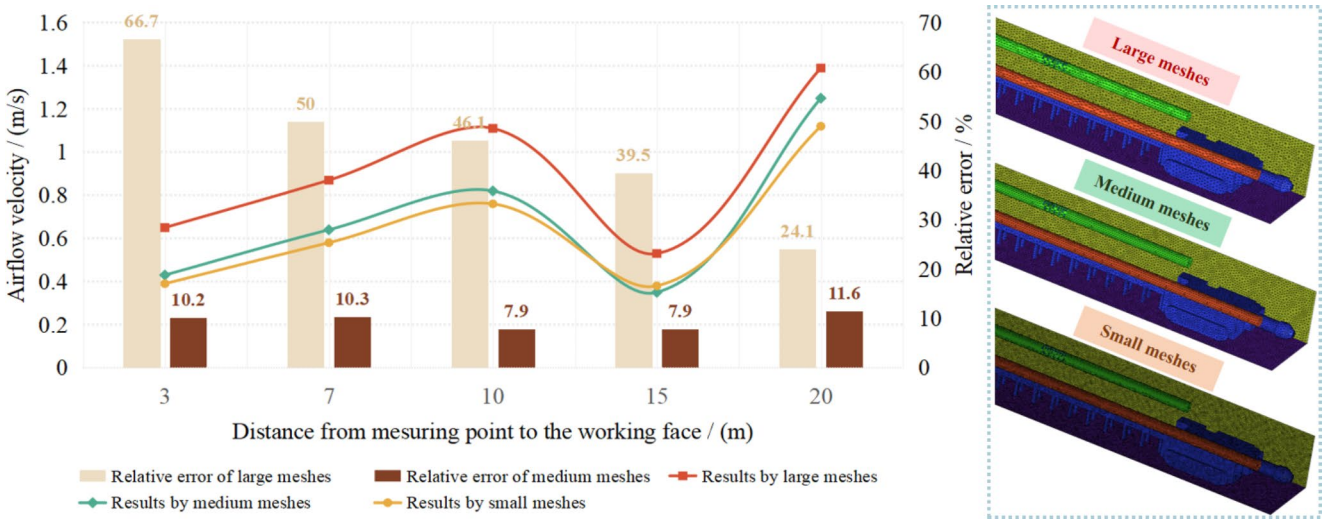

Fig. 3 Result of mesh independence test

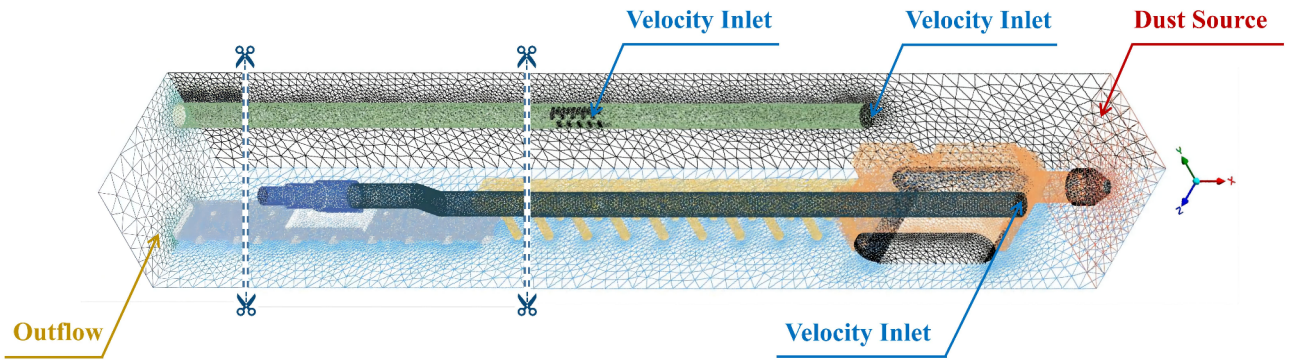

Fig. 4 Mesh and boundary conditions

The airflow velocities at the personnel breathing height in the cutting area, driver operation area, backrear of roadheader, duct overlapping area, and air curtain area, which were 3 m, 7 m, 10 m, 15 m, 20 m from the working face, were taken as the verification parameters.

The smaller the mesh size, the higher the accuracy of the simulation results obtained. Taking the airflow velocities under small mesh condition as the reference values, the relative errors of the results obtained from the large and the medium mesh were calculated. The result of mesh independence test is shown in Fig. 3. It can be seen that the airflow velocities show a same fluctuation rule, which indicates that all these three meshes are independent. However, there is a significant deviation in the result under large mesh condition, the average relative error reaches 45.3%, while the deviation under medium mesh condition is small, the average relative error is 9.6%. This illustrates that too much reduction in mesh size could not significantly improve the numerical simulation results. At the same time, too small mesh size will greatly increase the simulation workload, which not only takes longer time but also requires higher computer performance. Therefore, this study ultimately chose a medium mesh with a minimum size of 0.2 m for simulations.

3.2 Boundary conditions

The boundary conditions were set by ANSYS Fluent. As shown in Fig. 4, the surfaces of the outlet of the pressing air duct, the inlet of the extraction air duct and the radial jet ports of the wall-attached air duct were set as “velocity_inlet”; the surface of the end section of the tunnel was set as “outflow”; all other surfaces were set as “wall”. The working face was set as a dust generating surface.

4 Parameter settings

4.1 Airflow parameters

According to the measured values of the $63_{up}08$ fully mechanized working face, without the application of air curtain dust prevention technology, the airflow velocity at the outlet of the pressing air duct was about 10.6 m/s, and that at the inlet of the extraction air duct was about 9.9 m/s. To understand the influence of axial extraction velocity (v_e) on airflow structure, the values of v_e were set to 5 m/s, 10 m/s, and 15 m/s. According to the functional relationship between the air volume Q, the airflow velocity v, and the air duct section area A, that is $Q=vA$, the total amount of pressing air was approximately 320 m^3/min. The wall-attached air duct could adjust 50–90% pressing air to be ejected from the radial jet ports, the corresponding radial air volumes were 160 m^3/min, 192 m^3/min, 224 m^3/min, 256 m^3/min and 288 m^3/min. By the conversion between Q and v, the radial jet velocity (v_r) wa 7 m/s, 8 m/s, 9 m/s, 10 m/s and 12 m/s, respectively. To understand the impact of v_r on airflow structure, the values of v_r were selected as 8 m/s, 10 m/s and 12 m/s. According to the coal mine safety regulations, based on the cross-sectional area of the tunnel S, the extraction distance L should be less than $1.5 \cdot S^{1/2}$. The S of the $63_{up}08$ fully mechanized excavation tunnel is 21 m^2, resulting in $L<6.8$ m. To understand the influence of L on the airflow structure, the values of L were set to 2 m, 3 m, 4 m and 5 m.

4.2 Dust particle parameters

Dust samples were collected at $63_{up}08$ fully mechanized working face, and experimental tests were carried out on particle size distribution. On this basis, the basic parameters of particle phase in numerical simulation were set. The minimum diameter of dust particles was 0.82 μm, the median diameter was 4.83 μm, the maximum diameter was 26.5 μm. The mass flow rate was 0.0028 kg/s. In the DPM model, the particle time step was set to 0.01s, and the time step was set to 5000 to meet the maximum real-time process particle tracking. The maximum particle tracking step was set to 3200.

5 Model validation

In the $63_{up}08$ fully mechanized excavation tunnel, the original long pressure and short extraction local ventilation system has been applied. The measured parameters were: v_r=0 m/s, v_e=10 m/s, L=3 m. To verify the effectiveness of the model, the airflow velocity and dust concentration were measured by 9545-VELOCICALC (TSI Corporation, USA) and CCZG-2 A portable individual dust sampler (Shandong Shenhua Machinery Manufacturing Co. LTD, China). The measuring points were set at the miners' breathing height on the sidewalk. The measuring section was 5 m~30 m from the working face, every 5 m backward.

As shown in Figs. 5 and 6, the measured and simulation results were compared and analyzed.

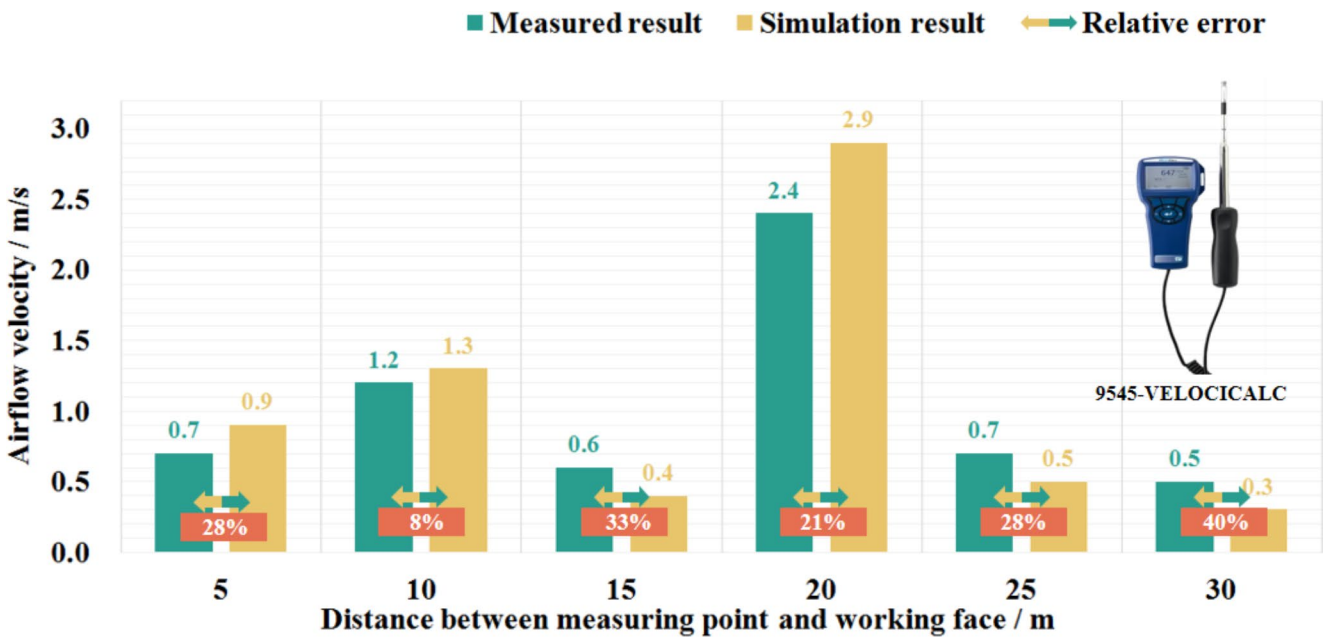

Fig. 5 Comparison of airflow velocity

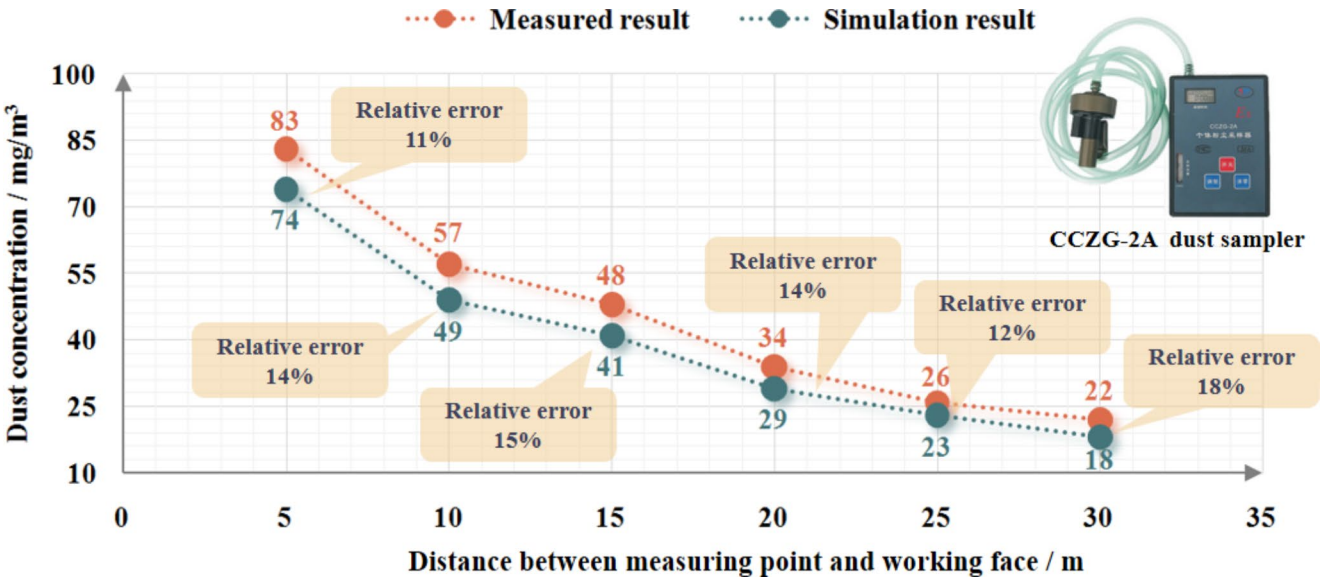

Fig. 6 Comparison of dust concentration

It can be seen that the variation trends of simulation values are substantially coincided with measured values. The average relative errors of airflow velocity and dust concentration are 26% and 14%, respectively. In engineering applications, the average relative error of about ± 20% between numerical simulation and experimental/test results is generally considered acceptable. Due to the complex environment in site, any artificial operation or change of production conditions can inevitably cause errors, therefore, the above relative errors are within the acceptable range.

6 Analysis of numerical simulation results

6.1 Airflow migration

Figures 7, 8 and 9 shows the airflow migrations under various v_r, v_e, and L conditions.

As shown in Fig. 7a, part of the pressing airflow is ejected radially from the wall-attached air duct at v_r=8 m/s, the radial jet impacts the wall on the extraction side of the tunnel and flows around the surface to form a wall jet. The residual pressing airflow is axially ejected from the outlet of the pressing air duct and migrates to the working face at the velocity of 2.2 m/s. After the axial jet collides with the working face, it converges towards the inlet of the extraction air duct under the negative pressure, forming a backflow that deviates from the working face. Due to the entrainment effect of the axial jet, part of the backflow is not sucked into the extraction air duct but is entrained into the axial jet, thus forming a circulating flow. It can affect the whole upper space of the roadheader. In this process, the wall jet is moving towards the working face, it converges into the axial jet as soon as it enters the working face. This results in inconsistent directions, significant differences in volumes and velocities of airflows in the working face. As shown in Figs. 7b and c with the increase of v_r, the volume and velocity of axial jet decrease, the entrainment effect weakens as well. Therefore, when v_r=10 m/s, the incidence of the circulating flow is reduced to less than 7 m from the working face. The deviation degree of the wall jet towards the axial jet is reduced. When v_r is further increased to 12 m/s, the axial jet velocity has been reduced to 0.5 m/s. At this time, the circulating flow cannot be formed in the working face, and the wall jet is directly moved to the inlet of the extraction air duct in the axial direction. Under this condition, the flow field in the working face shows an axial migration towards the working face. The differences in airflow volume and velocity between the pressing side and the extraction side are not large. The flow field distribution is uniform.

As shown in Fig. 8, when v_e=5 m/s, the extraction intensity in the working face is insufficient to allow the wall jet to migrate axially. The collision and disturbance between the radial airflow lead to the formation of turbulent flows in the overlapping region of air ducts. Under this condition, there is no additional inflow on the extraction side of the tunnel. Therefore, when the axial jet turns to the inlet of the extraction air duct, a “triangular windless zone” is formed. The triangular windless zone is a right-angled triangle with the boundary of the axial jet as the oblique edge, and the radial line of the outlet of the pressing air duct and the axial line of the boundary of the extraction air duct as the right-angled edges, respectively. In the triangular windless zone, the airflow velocity is less than 0.20 m/s, the distribution of airflow streamlines is extremely sparse. The volume and velocity of airflow on the pressing side differs greatly from

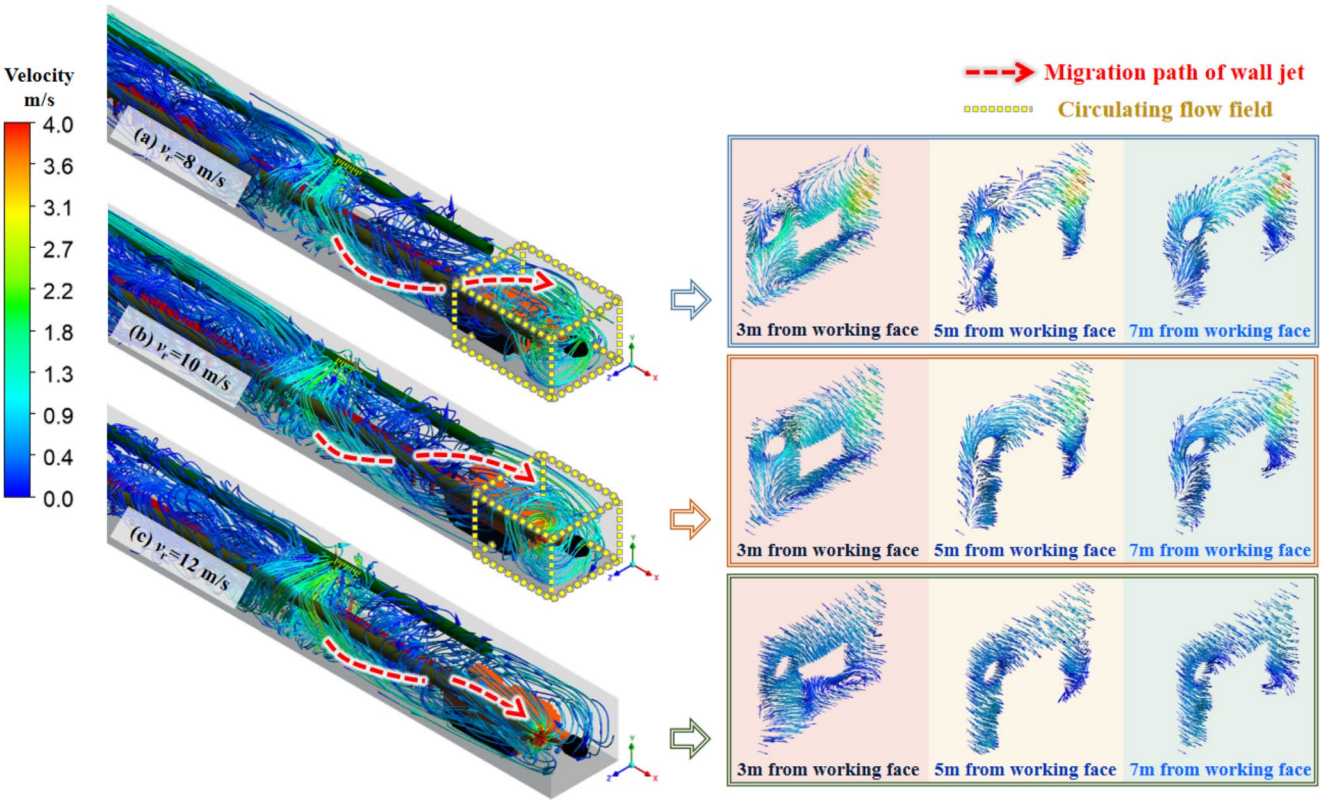

Fig. 7 Airflow migration under various v_r conditions

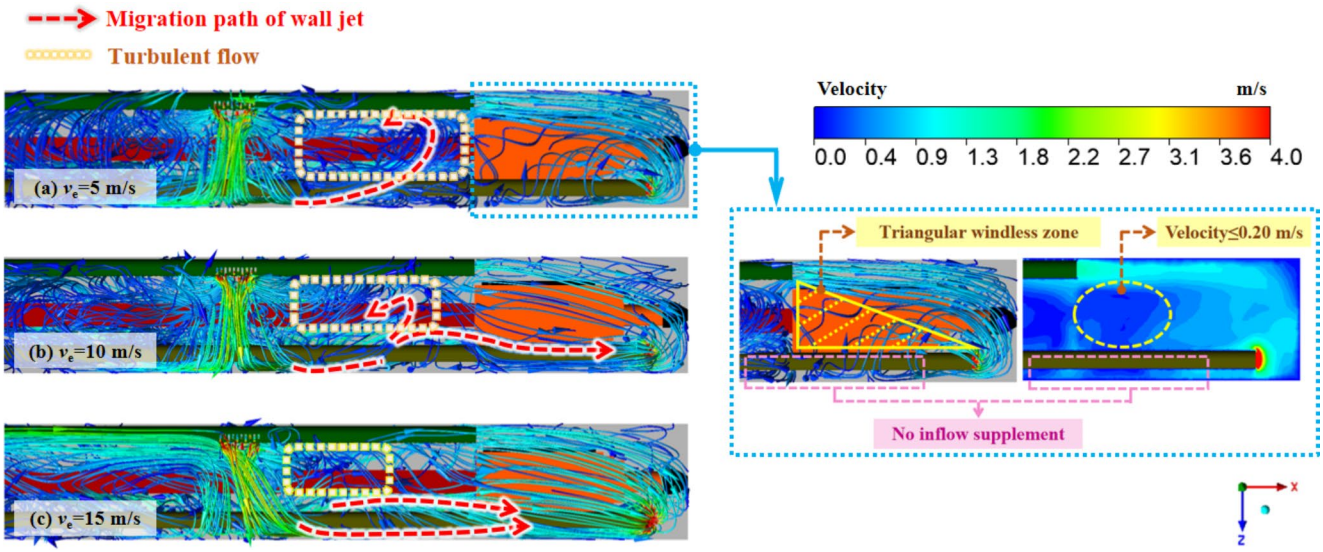

Fig. 8 Airflow migration under various v_e conditions

that on the extraction side. When v_e increases to 10 m/s, part of the wall jet starts an axial migration, supplementing the airflow on the extraction side. The range of turbulent flows is reduced. When v_e further increases to 15 m/s, almost all the wall jet migrates axially, the airflow in the working face realizes a complete uniform distribution.

As shown in Fig. 9, as L increases, the migration distance of the wall jet decreases. At the same time, the distance from the boundary of the axial jet to the working face increases. Both the above lead to the formation of a low-velocity turbulent flow field. The airflow velocity in this field is lower than 0.20 m/s. When L=2 m, the low-velocity turbulent flow field is at the turning corner in a triangular

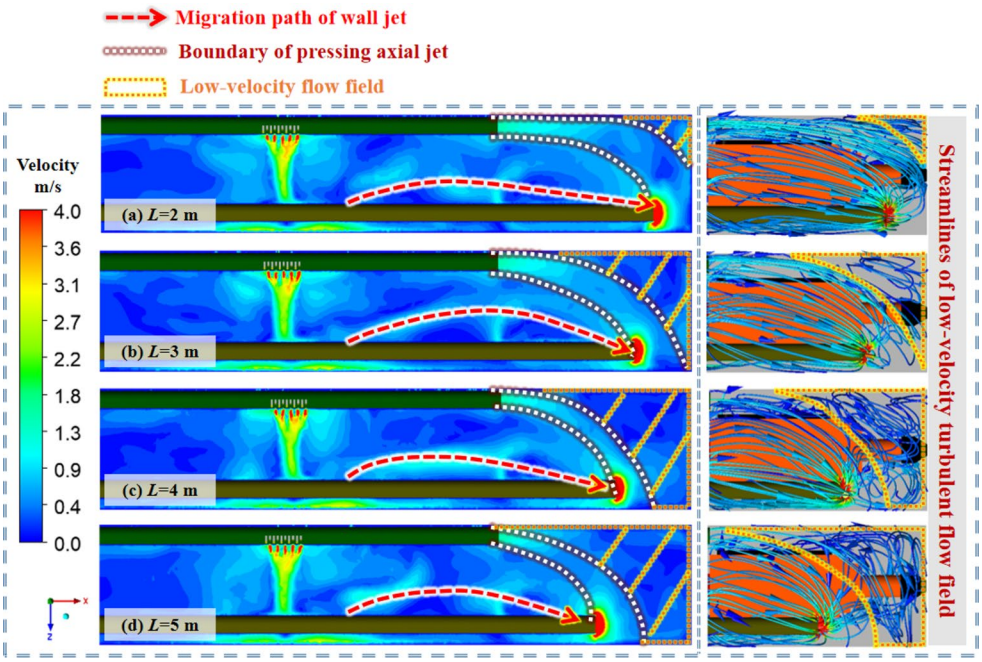

Fig. 9 Airflow migration under various L conditions

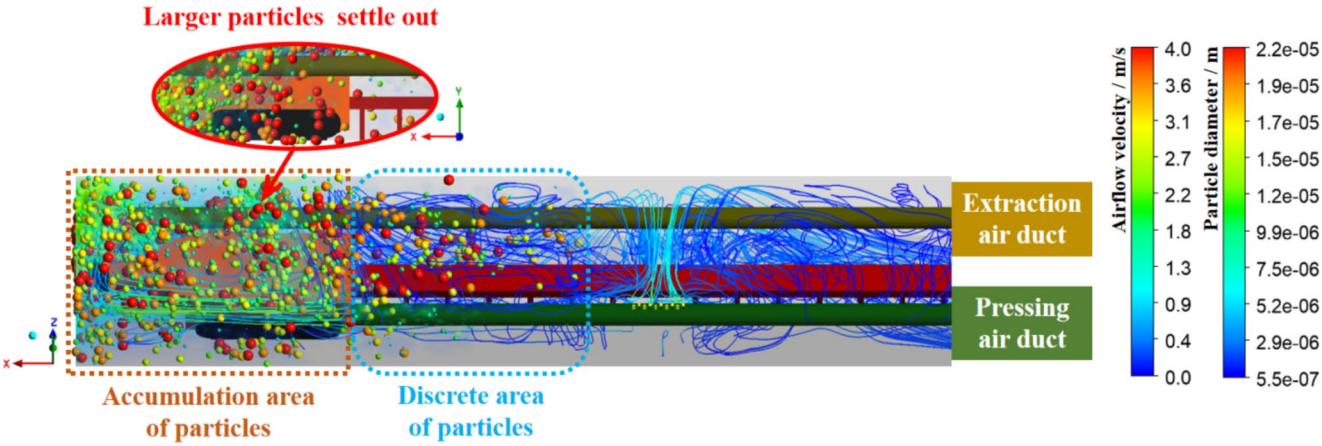

Fig. 10 Dust particle dispersion process

shape, the area is 3.32m^2. When L = 3 m, the area of the low-velocity turbulent flow field rapidly increases to 13.85m^2. As L increases to 4 m, the low-velocity turbulent flow field turns into a trapezoid shape, and the area further increases to 19.39m^2. When L further increases to 5 m, the area of the low-velocity turbulent flow field reaches to the maximum of 30.47m^2.

6.2 Dust diffusion

Figure 10 shows the dust particle dispersion process. It can be seen that an accumulation area of particles is formed within a certain range from the working face. In this area, a little part of large particles could settle out, more small particles are concentrated and suspended in the tunnel. Among these particles, some of them continue dispersing to the space outside the accumulation area and form a discrete area. In this area, the density of dust particles is significantly reduced, the particles are all suspended in the tunnel and can disperse to further place with the airflow.

Figures 11, 12 and 13 shows the dust particle distributions under various v_r, v_e, L conditions.

As shown in Fig. 11, when v_r=8 m/s, a circulating airflow field exists in the working face, a large number of dust particles in the sewage air return to the working face with the flow field, rather than continue to diffuse to other areas. The length of the accumulation area reaches 9.8 m, that of the discrete area reaches 10.4 m. With the increase of v_r, the circulating airflow field decreases, the dust diffusion distance decreases as well. When v_r=10 m/s, the length of the accumulation area decreases to 7.5 m, and that of the discrete area sharply decreases to 4.9 m. When v_r=12 m/s, the length

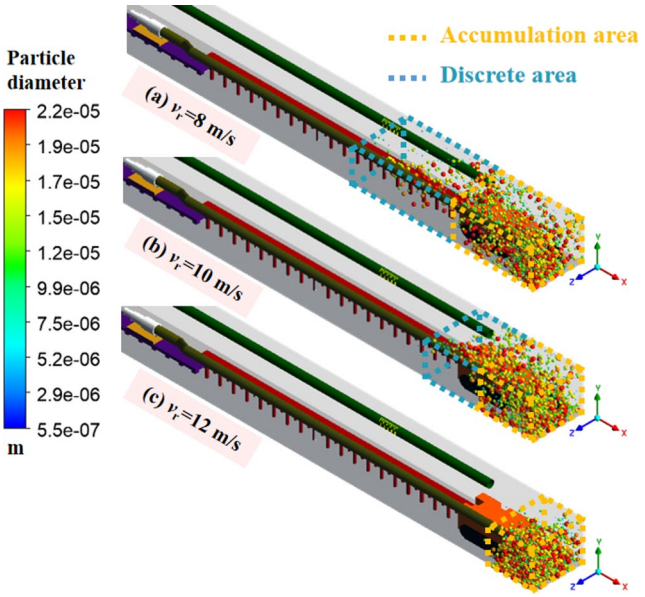

Fig. 11 Dust particle distributions under various v_r conditions

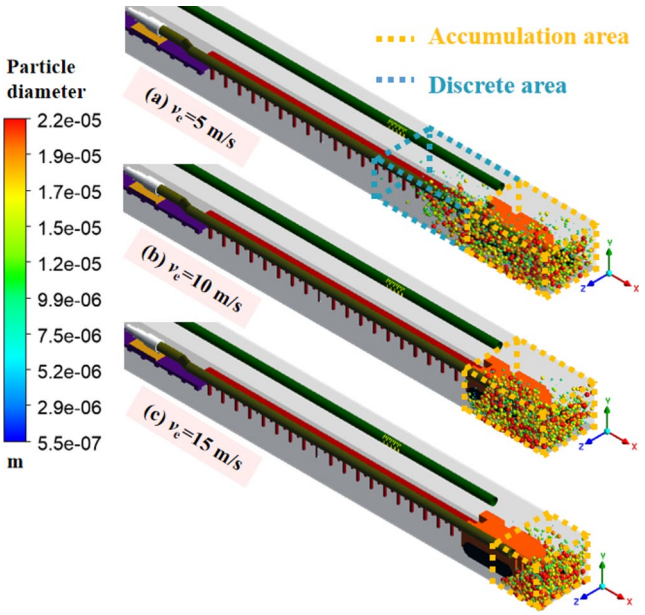

Fig. 12 Dust particle distributions under various v_e conditions

of the accumulation area decreases to 6.7 m and no discrete area is formed.

When v_e=5 m/s, there is a triangular windless zone in the working face. It makes the airflow volume and velocity on the pressing side are significantly higher than that on the extraction side. Therefore, as shown in Fig. 12, the dust particles are concentrated on the extraction side and constantly diffuse to the rear space of the roadheader. The length of the accumulation area is 9.6 m, and that of the discrete area is 9.8 m. With the increase of v_e, the distribution of airflow volume and velocity becomes uniform, and the dust

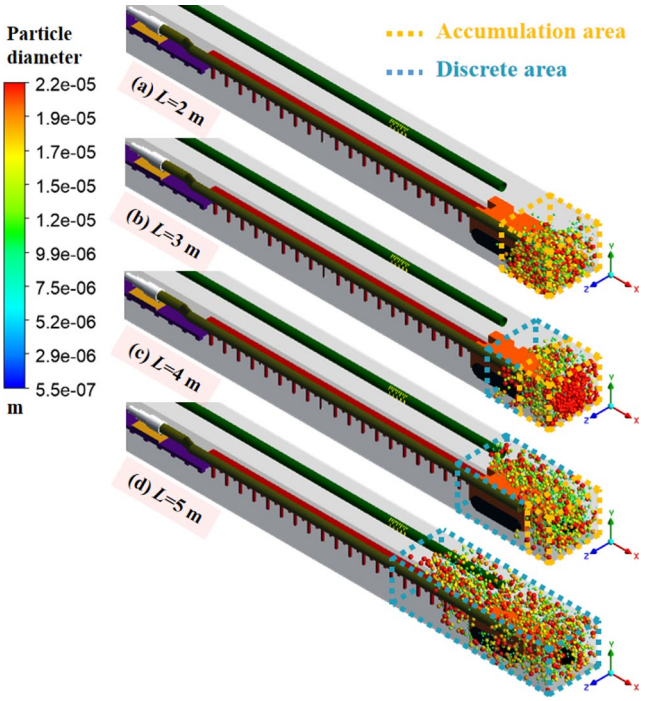

Fig. 13 Dust particle distributions under various L conditions

prevention ability increases accordingly. When v_e=10 m/s, no discrete area is formed, and the length of the accumulation area does not change significantly. When v_e further increases to 15 m/s, the length of the accumulation area rapidly decreases to 6.2 m.

As L increases, the area of the low-velocity turbulent flow field increases. It creates favorable conditions for dust diffusion. Therefore, as shown in Fig. 13, the length of the discrete area increases, while that of the accumulation area decreases. When L=2 m, the length of the accumulation area is 6.7 m.There is no discrete area formed. When L=4 m, the length of the accumulation area has decreased to 2.4 m, that of the discrete area increases to 8.9 m. When L further increases to 5.0 m, there is a significant large-scale dispersion of dust particles. No accumulation area is formed, the length of the discrete area has reached as high as 16.9 m.

It can be seen that with the increase of v_r and v_e, with the decrease of L, the dust pollution range continues decreasing, indicating that the dust prevention ability of the airflow field is strengthened. During the diffusion of dust particles, the range of the discrete area decreases sharply, until the dust particles are all concentrated in the accumulation area.

7 Field application

A wall-attached air duct was installed in the $63_{up}08$ fully mechanized tunnel. Based on the rules obtained from numerical simulation, the v_r was optimized to 12 m/s; the

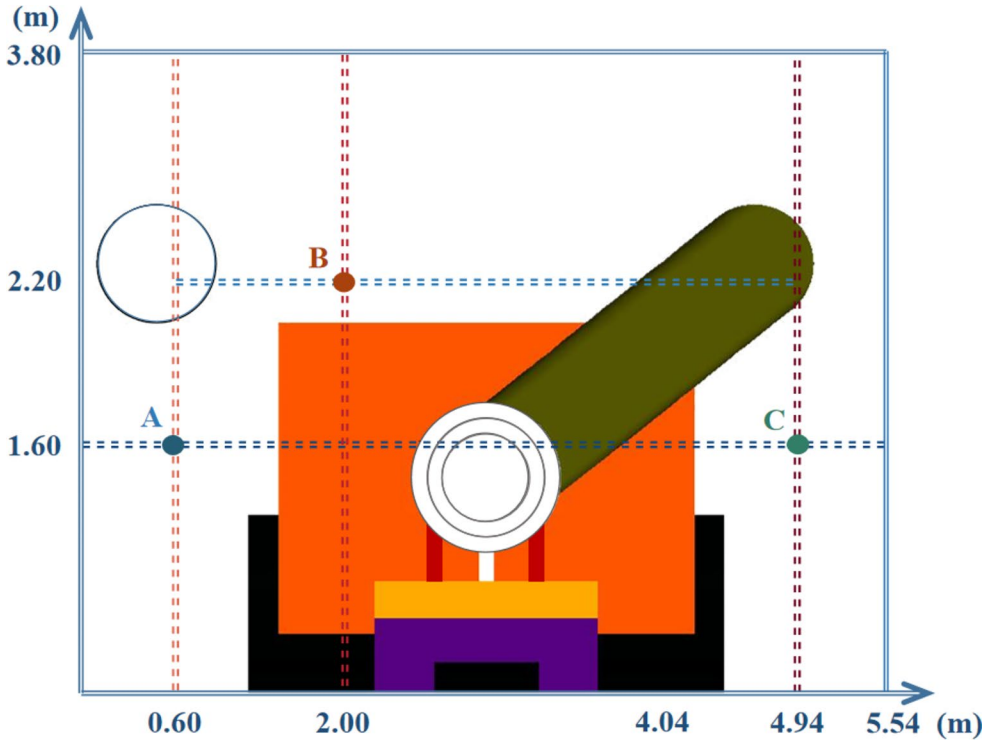

Fig. 14 Measuring points

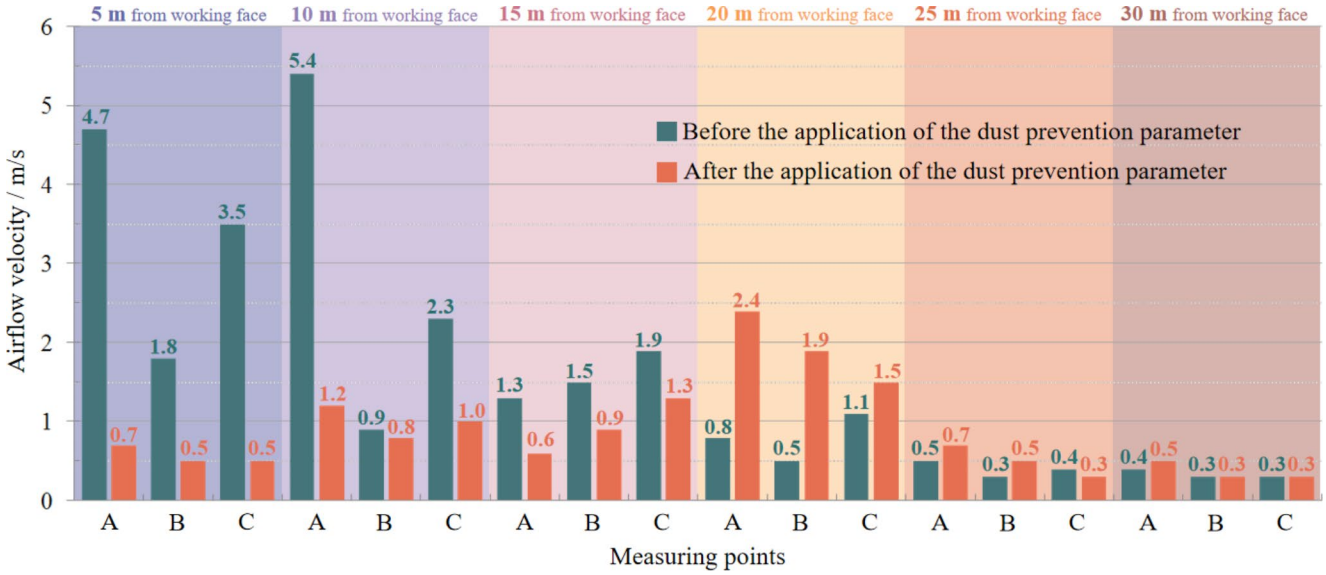

Fig. 15 Airflow velocities before and after applying the optimized parameters

v_e was optimized to the maximum of 13 m/s; and the L was optimized to 2 m. According to the measuring sections set for model validation, as shown in Fig. 14, three measuring points were arranged in each measuring section. The measured airflow velocity and dust concentration at each section before and after applying the optimized parameters are shown in Figs. 15, 16 and 17. The actual dust dispersion in site is shown in Fig. 18.

It can be seen from Figs. 15, 16, 17 and 18 that:

Before applying the optimized parameters, the airflow velocities in sections 5 m and 10 m from the working face differ greatly, indicating that the airflow distribution is uneven. The airflow velocity at point A is as high as 4.7 m/s and 5.4 m/s, respectively. They are far beyond the effective dust prevention velocity range. Under this condition, the dust concentration at point C is significantly higher than that at point A and B. The average dust concentration in the front section of the driver is as high as 326 mg/m^3. Even in

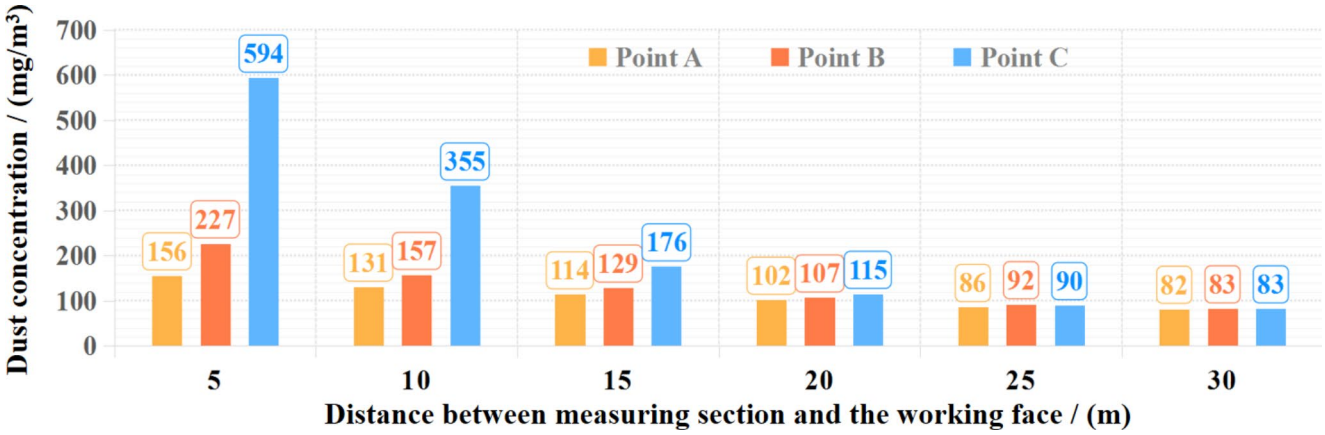

Fig. 16 Dust concentration before applying the optimized parameters

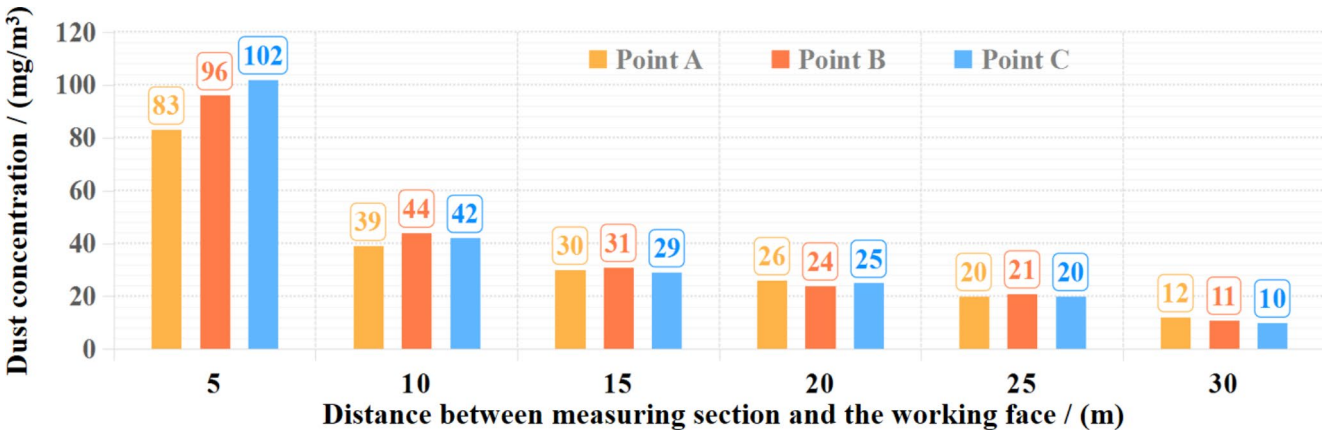

Fig. 17 Dust concentration after applying the optimized parameters

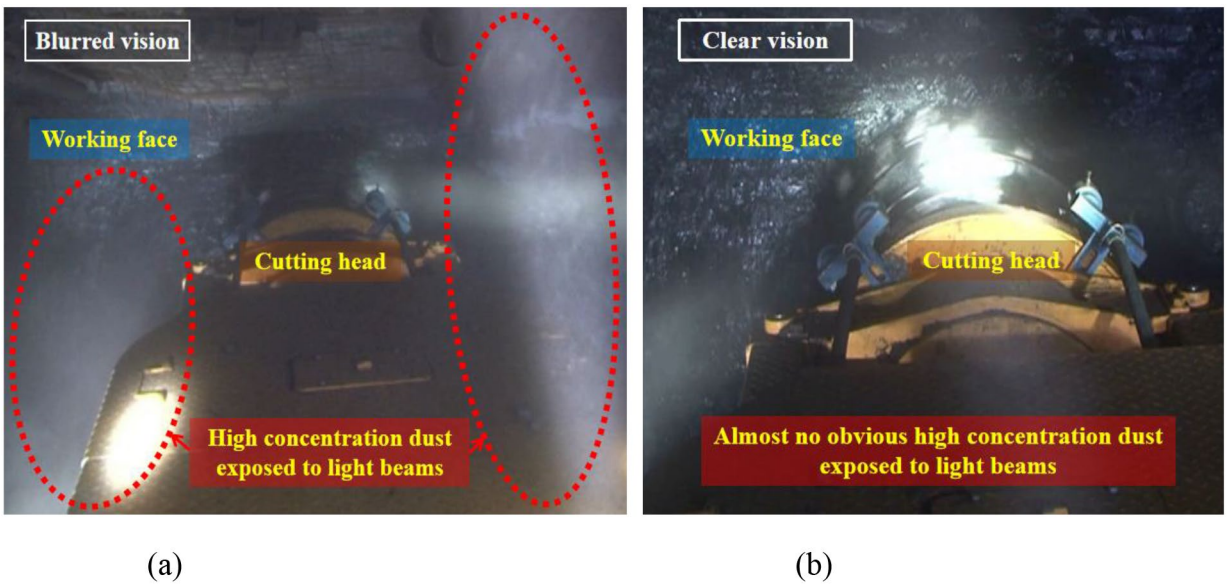

Fig. 18 Dust dispersions before and after applying the optimized parameters **a** Before the application **b** After the application

the section 20 m from the working face, the average dust concentration can still be 108 mg/m^3.

After applying the optimized parameters, airflow velocities in sections 5 m and 10 m from the working face are similar, indicating that the airflow velocity distribution is uniform. The dust concentration at each section decreases significantly. The average dust concentration in the front section of the driver reduces to 94 mg/m^3, the average dust removal efficiency increases by 71%. In the section. 15 m from the working face, the dust concentration has reduced to less than 50 mg/m^3. It means that high concentration dust pollution has been effectively prevented, and the working environment for operators is significantly improved.

8 Conclusions

In this study, the proportional physical model of $63_{up}08$ excavation tunnel was established and validated. The airflow structure evolutions and dust particle diffusions under various v_r, v_e and L conditions were simulated and analyzed. The main conclusions are as follows:

(1) As v_r, v_e increase and L decreases, the migration path of the wall jet changes to the axial direction. The airflow distribution in the working face tends to be uniform.
(2) An accumulation area and a discrete area are formed during dust dispersion. With the increase of v_r, v_e, and with the decrease of L, the range of the discrete area decreases, until dust particles are all concentrated in the accumulation area.
(3) According to the simulation result, the ventilation parameters were optimized to v_r=12 m/s, v_e=13 m/s, L=2 m. After the application of these parameters, the average dust removal efficiency at the driver's position increases by 71%. The working environment for operators can be effectively improved.

Acknowledgements This work was financially supported by the Natural Science Foundation of Shandong Province (ZR2020QE124, ZR2023ME031 and ZR2023ME012); Innovation Achievement Cultivation Project of Qingdao University of Technology (CLZ2022-002); National Natural Science Foundation of China (52404222 and 52374209).

Author contributions Hao Wang: Conceptualization, Validation, Investigation, Writing - original draft, Methodology. Chuangye Xin: Methodology, Investigation, Formal analysis, Writing - original draft. Shouqing Lu: Formal analysis, Writing - original draft, Supervision. Yongliang Zhang: Formal analysis, Validation, Writing -review & editing. Zhanyou Sa: Writing -review & editing, Data curation, Supervision. Jinxu Tao: Writing -review & editing, Data curation. Zhuang Liu: Writing -review & editing, Data curation.

Declarations

Competing interests The authors declare that they have no known competing financial interests or personal relationships that could have appeared to influence the work reported in this paper.

Open Access This article is licensed under a Creative Commons Attribution 4.0 International License, which permits use, sharing, adaptation, distribution and reproduction in any medium or format, as long as you give appropriate credit to the original author(s) and the source, provide a link to the Creative Commons licence, and indicate if changes were made. The images or other third party material in this article are included in the article's Creative Commons licence, unless indicated otherwise in a credit line to the material. If material is not included in the article's Creative Commons licence and your intended use is not permitted by statutory regulation or exceeds the permitted use, you will need to obtain permission directly from the copyright holder. To view a copy of this licence, visit http://creativecommons.org/licenses/by/4.0/.

References

Agioutanti E, Keles C, Sarver E (2020) A thermogravimetric analysis application to determine coal, carbonate, and non-carbonate minerals mass fractions in respirable mine dust. Appl Occup Environ Hyg 17:1–12

Animah F, Keles C, Reed R. W, Sarver E (2024) Effects of dust controls on respirable coal mine dust composition and particle sizes: case studies on auxiliary scrubbers and canopy air curtain. Int J Coal Sci Technol 11(33). https://doi.org/10.1007/s40789-024-00688-8

Aznar-Sánchez JA, Velasco-Muñoz JF, Belmonte-Ureña LJ, Manzano-Agugliaro F (2019) Innovation and technology for sustainable mining activity: a worldwide research assessment. J Clean Prod 221:38–54

Cheng W, Wang H, Nie W, Zhou G, Sun B (2016) Impact of pressure pumping ratio and location of air curtain generator on the dust resistance effect in fully mechanized workface. J China Coal Soc 41(8):1976–1983

Ding W (2020) ANSYS fluent Fluid Computing: from beginner to Proficient. China Machine, Beijing

Ding C, He X, Nie B (2017) Numerical simulation of airflow distribution in mine tunnels. Int J Min Sci Technol 27:663–667

Fan L, Liu S (2021) Respirable nano-particulate generations and their pathogenesis in mining workplaces: a review. Int J Coal Sci Technol 8(2):179–198

Gao R, Wang P, Li Y, Liu R (2021) Determination of optimal blowing-to-suction flow ratio in mechanized excavation face with wall-mounted swirling ventilation using numerical simulations. Int J Coal Sci Technol 8(2):248264

Ge S, Liu J, Zhang Y (2003) Model and application for flow field of tapered windscreen fan. J Liaoning Tech Univ 22(S1):77–80

Geng F, Luo G, Wang Y, Peng Z, Hu S, Zhang T, Chai H (2018) Dust dispersion in a coal roadway driven by a hybrid ventilation system: a numerical study. Process Saf Environ Prot 113:388–400

Geng F, Gui C, Wang Y, Zhou F, Hu S, Luo G (2019) Dust distribution and control in a coal roadway driven by an air curtain system: a numerical study. Process Saf Environ Prot 121:32–42

Gu D, Li Q (2021) Theoretical framework and key technologies of underground ecological protection based on coal mine occupational health prevention. J China Coal Soc 46(03):950–958

Guyonnaud L, Solliec C, Dufresne de Virel M, Rey C (2000) Design of air curtains used for area confinement in tunnels. Exp Fluids 28:377–384

Hu S, Liao Q, Feng G, Huang Y, Shao H, Fan Y, Ye Y (2019) Numerical study of gas-solid two-phase flow around road-header drivers in a fully mechanized excavation face. Powder Technol 344:959–969

Hua Y, Nie W, Liu Q, Peng H, Wei W, Cai P (2020) The development and application of a novel multi-radial-vortex-based ventilation system for dust removal in a fully mechanized tunneling face. Tunneling Undergr Space Technol 98:103253

Jiang H, Luo Y (2021) Development of a roof bolter drilling control process to reduce the generation of respirable dust. Int J Coal Sci Technol 8(2):199–204

Jiang Z, Yan P, Chen J, Zhang Z (2015) Optimization on parameters of long distance forced and short distance ventilation system in mine rock heading roadway. Coal Sci Technol 43:54–58

Kumar RA, Gupta N, Schafrik S (2022) CFD modeling and laboratory studies of dust cleaning efficacy of an efficient four stage non-clogging impingement filter for flooded-bed dust scrubbers. Int J Coal Sci Technol 9(1):16

Kurnia JC, Sasmito AP, Hassani FP, Mujumdar AS (2015) Introduction and evaluation of a novel hybrid brattice for improved dust control in underground mining faces: a computational study. Int J Min Sci Technol 25:537–543

Li M, Aminossadati SM, Wu C (2016) Numerical simulation of air ventilation in super-large underground developments. Tunn Undergr Space Technol 52:38–43

Li S, Xie B, Hu S, Jin H, Liu H, Tan X, Zhou F (2019a) Removal of dust produced in the roadway of coal mine using a mining dust filtration system. Adv Powder Technol 30(5):911–919

Li Y, Wang P, Liu R, Gao R (2019b) Optimization of structural parameters and installation position of the wall-mounted air cylinder in the fully mechanized excavation face based on CFD and orthogonal design. Process Saf Environ Prot 130:344–358

Lodhia S, Hess N (2014) Sustainability accounting and reporting in the mining industry: current literature and directions for future research. J Clean Prod 84:43–50

Lu S, Li M, Sa Z, Liu J, Wang S, Qu M (2022) Discrimination of gas diffusion state in intact coal and tectonic coal: Model and experiment. Fuel 325:124916

Magesh T, Zheng Y, Tien JC (2016) DPM simulation in an underground entry: comparison between particle and species models. Int J Min Sci Technol 26:487–494

Nie W, Wei W, Liu Y, Chen L, Cheng W, Ma X (2016) Research on dust control and removal method of multi-direction rotational air curtain at rock mechanized excavation face and its application. J Cent South Univ (Science Technology) 47(10):3612–3619

Nie W, Sun N, Liu Q, Guo L, Xue Q, Liu C, Niu W (2022) Comparative study of dust pollution and air quality of tunnelling anchor integrated machine working face with different ventilation. Tunn Undergr Space Technol 122:104377

Parra MT, Villafruela JM, Castro F, Mendez C (2006) Numerical and experimental analysis of different ventilation systems in deep mines. Build Environ 41(2):87–93

Ren W, Shi J, Zhu J, Guo Q (2020) An innovative dust suppression device used in underground tunneling. Tunn Undergr Space Technol 99:103337

Shekarian Y, Rahimi E, Shekarian N, Rezaee M, Pedram R (2021) An analysis of contributing mining factors in coal workers' pneumoconiosis prevalence in the United States coal mines, 1986–2018. Int J Coal Sci Technol 8(6):1227–1237

Shi G, Liu M, Guo Z, Hu F, Wang D (2017) Unsteady simulation for optimal arrangement of dedusting air duct in coal mine heading face. J Loss Prev Process Ind 46:45–53

Trechera P, Querol X, Lah R, Johnson D, Wrana A, Williamson B, Moreno T (2022) Chemistry and particle size distribution of respirable coal dust in underground mines in Central Eastern Europe. Int J Coal Sci Technol 9(1):3

Wang H, Nie W, Cheng W, Liu Q, Jin H (2018) Effects of air volume ratio parameters on air curtain dust suppression in a rock tunnel's fully-mechanized working face. Adv Powder Technol 29:230–244

Wang P, Li Y, Liu R, Shi Y (2019a) Effects of forced-to-exhaust ratio of air volume on dust control of wall-attached swirling ventilation for mechanized excavation face. Tunneling Undergr Space Technol 90:194–207

Wang Z, Li S, Ren T, Wu J, Lin H, Shuang H (2019b) Respirable dust pollution characteristics within an underground heading face driven with continuous miner-a CFD modelling approach. J Clean Prod 217:267–283

Wang H, Cheng W, Sa Z, Liu J, Zhang R, Chen D (2021a) Experimental study of the effects of air volume ratios on the air curtain dust cleaning in fully mechanized working face. J Clean Prod 293:126109

Wang H, Sa Z, Cheng W, Zhang R, Yang S (2021b) Effects of forced-air volume and suction region on the migration and dust suppression of air curtain during fully mechanized tunneling process. Process Saf Environ Prot 145:222–235

Yin S, Nie W, Liu Q, Hua Y (2019) Transient CFD modeling of space-time evolution of dust pollutants and air-curtain generator position during tunneling. J Clean Prod 239:17924

Yin S, Nie W, Guo L, Liu Q, Hua Y, Cai X, Cheng L, Yang B, Zhou W (2020) CFD simulations of air curtain dust removal effect by ventilation parameters during tunneling. Adv Powder Technol 31(6):2456–2468

Zhang J, Zhu T, Gao M, Li K (2011) Parameter optimization and numerical simulation of dust-collecting and dedusting system with air curtain in heading face. Adv Mater Res 317–319:2073–2078

Zhang G, Zhou G, Song S, Zhang L, Sun B (2020) CFD investigation on dust dispersion pollution of down/upwind coal cutting and relevant countermeasures for spraying dustfall in fully mechanized mining face. Adv Powder Technol 31(8):3177–3190

Zhang G, Sun B, Song S, Wang H, Zhou G (2021) CFD comparative analysis on the pollution characteristics of coal dust under turbulent airflow from coal cutting in the fully mechanized mining face. Process Saf Environ Prot 146:515–530

Zhou G, Zhang Q, Hu Y, Gao D, Wang S, Sun B (2020) Dust removal effect of negatively-pressured spraying collector for advancing support in fully mechanized coal mining face: numerical simulation and engineering application. Tunn Undergr Space Technol 95:103149

Publisher's note Springer Nature remains neutral with regard to jurisdictional claims in published maps and institutional affiliations.